

# Comprehensive Analysis of the Transient X-ray Pulsar MAXI J1409-619

Ç. K. Dönmez<sup>1</sup>★, M.M. Serim<sup>1,2</sup>, S. Ç. İnam<sup>3</sup>†, Ş. Şahiner<sup>4</sup>, D. Çerri-Serim<sup>1</sup>  
and A. Baykal<sup>1</sup>‡

<sup>1</sup>*Physics Department, Middle East Technical University, 06531 Ankara, Turkey*

<sup>2</sup>*TÜBİTAK ULAKBİM, 06510 Ankara, Turkey*

<sup>3</sup>*Department of Electrical and Electronics Engineering, Başkent University, 06790 Ankara, Turkey*

<sup>4</sup>*Department of Electronics and Communication Engineering, Beykent University, 34398 İstanbul, Turkey*

Accepted XXX. Received YYY; in original form ZZZ

## ABSTRACT

We probe the properties of the transient X-ray pulsar MAXI J1409-619 through RXTE and SWIFT follow up observations of the outburst in 2010. We are able to phase connect the pulse arrival times for the 25 days episode during the outburst. We suggest that either an orbital model (with  $P_{orb} \approx 14.9(7)$ ) or a noise process due to random torque fluctuations (with  $S_r \approx 1.3 \times 10^{-18} \text{ Hz s}^{-2}$ ) is plausible to describe the residuals from our timing solution. The frequency derivatives indicate a positive torque-luminosity correlation, implying a temporary accretion disc formation during the outburst. Utilizing standard accretion disc theory, we estimate the dipolar magnetic field strength as  $\approx 2.9 \times 10^{11}$  Gauss and the inner disc radius as about  $4.8 \times 10^8$  cm. We also discover several quasi-periodic oscillations (QPOs) with their harmonics whose centroid frequencies decrease as the source flux decays. Assuming QPO frequencies match with Keplerian frequencies at the inner disc, we obtain compatible inner radius and dipolar magnetic field strength values deduced from torque-luminosity relation. The pulse fraction of the source exhibits a positive correlation with the source count rates up to a critical point after which correlation turns out to be negative. We also present spectral analysis of the source. From RXTE-PCA observations, spectrum is found to be softer when the luminosity is lower than about  $5 \times 10^{36} \text{ ergs s}^{-1}$ . From pulse phase spectroscopy, we have also shown that the phases with lower flux tend to be spectrally softer.

**Key words:** stars: neutron - pulsars: : individual: MAXI J1409-619 - accretion, accretion discs

## 1 INTRODUCTION

MAXI J1409-619 is a transient pulsar in a high mass X-ray binary (HMXB) system which was discovered by the Gas Slit Camera (GSC), being one of the detectors of the Monitor of All-sky X-ray Image (MAXI) experiment, on 2010 October 17, with a  $(41 \pm 7)$  mCrab peak flux in 4–10 keV (Yamaoka et al. 2010). Using Neil Gehrels Swift Observatory’s (SWIFT) X-ray Telescope (XRT) observations, Kennea et al. (2010a) reported the source location as RA =  $14^h 08^m 02.56^s$ , Dec. =  $-61^\circ 59' 00.3''$  in J2000 coordinates, but no optical counterpart could be found. On 2010 November 30, when MAXI J1409-619 underwent an outburst becoming  $\sim 7$  times brighter compared to its initial observations, SWIFT Burst Alert Telescope (BAT) was triggered to observe the source, revealing a  $503 \pm 10$  s periodicity with 42% sinusoidal peak-to-through modulation (Kennea et al. 2010b). Routine MAXI/GSC observations indicated that the source was brightened significantly between 2010 November 25–December 3 (Ueno et al. 2010). Utilizing the FERMI Gamma-ray Burst Monitor (GBM) observations on 2010 December 2-3; the source period was refined as 506.93(5)s, the frequency derivative of  $\dot{\nu} = 1.66(14) \times 10^{-11}$  Hz/s was found and the double-peaked nature of the pulse profile was revealed (Camero-Arranz et al. 2010). The spectra obtained from the Rossi X-ray Timing Explorer (RXTE) -Proportional Counter Array (PCA) observations were modelled by a cut-off power law with either partially covered absorption or reflection and a narrow iron line in both cases, with no sign of cyclotron absorption. In both models, the photon index was found to be  $\Gamma \approx 1.3$  (Yamamoto et al. 2010). Kaur et al. (2010) announced the detection of a QPO at  $0.192 \pm 0.006$  Hz with 2 harmonics, using a total of 20 ks of observations of 2010 December 11. From archival observations of BeppoSAX, The Advanced Satellite for Cosmology and Astrophysics (ASCA), INTERnational Gamma-Ray Astrophysics Laboratory (INTEGRAL), it was inferred that MAXI J 1409-619 was in a low state during the observations prior to its discovery (Sguera et al. 2010; Orlandini et al. 2012).

In this paper, we will present results of comprehensive timing and spectral analysis of MAXI J1409-619, using the observations of RXTE and Swift observatories. In Section 2, we give a brief

\* E-mail: cagatay.donmez@metu.edu.tr

† E-mail: inam@baskent.edu.tr

‡ E-mail: altan@astroa.physics.metu.edu.tr

information about the observations and data reduction. In Section 3, we present our timing and spectral analysis. In Section 4, we summarize and discuss our results.

## 2 OBSERVATIONS AND DATA REDUCTION

### 2.1 Observations

#### 2.1.1 RXTE-PCA

RXTE, launched on 1995 December 30 and operational until 2012, was an observatory satellite dedicated to X-ray astronomy. PCA instrument onboard RXTE consisted of five identical proportional counter units (PCU), each of which had an effective area of  $\sim 1300 \text{ cm}^2$  (Jahoda et al. 1996). Each PCU was able to detect up to  $20\,000 \text{ cts s}^{-1}$  (Jahoda et al. 2006). PCA had an energy range of 2–60 keV, 256 energy channels and  $1^\circ$  FoV.

RXTE PCA observations of MAXI J1409-619 took place between 2010 October 22 and 2011 February 5 (corresponding to the observation sets with proposal numbers 95358, 95441, 96410). A total of 50 observations are used in our analysis, amounting a total exposure of 135.0 ks. *Standard-2* mode data are used for extracting spectra (16 s timing resolution), and *Good Xenon* mode data are used for extracting lightcurve ( $\sim 1 \mu\text{s}$  timing resolution).

#### 2.1.2 SWIFT-XRT

SWIFT is a multi-wavelength space observatory, launched on 2004 November 20. SWIFT is mainly used for gamma-ray burst monitoring, yet it also proved its effectiveness in X-ray astronomy through onboard 3.5-meter X-ray telescope XRT operating in 0.2–10 keV energy range. XRT has a  $110 \text{ cm}^2$  effective area and 18 arcsec half-power diameter resolution (Gehrels et al. 2004).

SWIFT-XRT made 32 observations of MAXI J1409-619 between 2010 October 20 and 2011 January 28. Of these observations, 13 of them are conducted in photon counting (PC) mode, 17 of them in window timing (WT) mode and 2 of them utilizes both modes. WT mode has 1.8 ms high timing resolution but keeps only one dimensional imaging data, whereas PC mode retains full spectroscopy and  $600 \times 602$  pixels imaging information but with only 2.5 s timing resolution (Burrows et al. 2005). Our analysis utilize the PC mode observations, each of which spans  $\sim 1$ –2 ks, leading to a total exposure of 19.3 ks.

## 2.2 Data Reduction

Data reduction was conducted using HEASOFT v6.22.1. Raw SWIFT-XRT data are reprocessed by the standard pipeline tool XRTPipeline v0.13.4. Then, the source counts are selected with a 20 pixel radius circle. Background subtraction and pile-up corrections are performed. Afterwards, Solar System barycentre corrections are applied to the data. First 30 channels of XRT data, corresponding to  $<0.3$  keV are marked "bad" as XRT is not considered reliable below this energy range. The spectra are rebinned through GRPPHA in such a way that there are at least 20 counts per bin.

In order to process RXTE PCA data, good time intervals are selected. In reference to the source count rates, Epoch 5C background models obtained provided by the RXTE Guest Observer Facility are used for background spectra and lightcurve which is created with 0.125 s bin size. Lightcurve count rates are corrected to total number of active PCUs and Solar System barycentric correction is applied. Only PCU 2 data are used for spectral analysis. The energy range used for spectral analysis is 3–25 keV, and 0.5% systematic error is applied to long and combined observations.

## 3 DATA ANALYSIS

### 3.1 Timing Analysis

### 3.2 Pulse Timing, Timing Solution and Torque Noise

In the timing analysis, we use background subtracted and Solar System barycenter corrected 0.125 s binned RXTE–PCA lightcurve of the source. In order to represent the long term evolution of the source count rates, the 1-day binned lightcurve is shown in Figure 1.

We fold the resulting lightcurve at frequencies measured through FERMI GBM pulsar project <sup>1</sup>. We also search for the best frequencies by using statistically independent trial frequencies (Leahy et al. 1983). Our search of best frequencies is consistent with the pulse frequencies provided by FERMI GBM pulsar project team. We construct the pulse profiles with 20 phase bins and cross-correlate each with the template pulse. In the cross correlation analysis, we use the harmonic representation of pulses (Deeter & Boynton (1985), see also İçdem et al. (2012) for applications).

We are able to phase connect all pulse arrival times during the outburst. We fitted pulse arrival times to the cubic polynomial,

$$\delta\phi = \delta\phi_o + \delta\nu(t - t_o) + \frac{1}{2}\dot{\nu}(t - t_o)^2 + \frac{1}{6}\ddot{\nu}(t - t_o)^3 \quad (1)$$

<sup>1</sup> <https://gammaray.nsstc.nasa.gov/gbm>

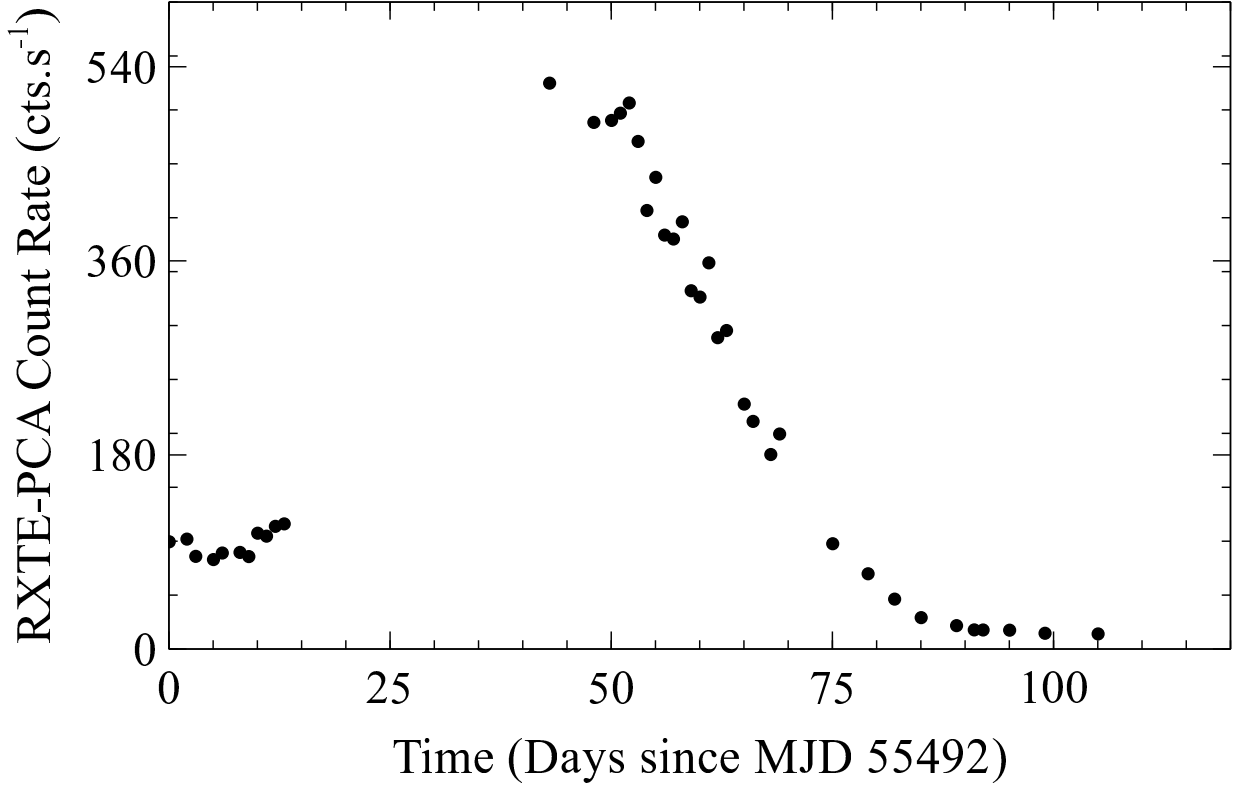


Figure 1. 2-60 keV 1-day binned RXTE-PCA lightcurve of MAXI J1409-619.

where  $\delta\phi$  is the pulse phase offset found from the pulse timing analysis,  $t_o$  is the epoch for folding;  $\delta\phi_o$  is the residual phase offset at  $t_o$ ;  $\delta\nu$  is the correction to the pulse frequency at time  $t_0$ ;  $\dot{\nu}$  is the first time derivative of pulse frequency,  $\ddot{\nu}$  is the second time derivative of pulse frequency. In Fig. 2, we present the pulse phases and the residuals of the pulse arrival times after the removal of a cubic polynomial. It should be noted that during the outburst, luminosity (or mass accretion rate) is increasing in time, so pulse frequency derivative is affected accordingly. Therefore cubic polynomial fitting to the pulse arrival times describes pulse arrival times better than a quadratic fitting.

The residuals after cubic polynomial fit in Fig. 2 is well fitted to the circular orbital model with a period of 14.9(7) days. The orbital model has decreased reduced  $\chi^2$  from  $\sim 35$  to  $\chi^2 \sim 1$ . The timing and possible orbital parameters obtained by the models are listed in Table 1. Using these orbital parameters, the mass function of the system can be deduced as;

$$f(M) = \frac{4\pi^2(a_x \sin i)^3}{GP_{orb}^2} = \frac{(M_c \sin i)^3}{(M_x + M_c)^2} \sim 0.1M_{\odot}, \quad (2)$$

which indicates that MAXI J1409-619 should have a small inclination angle.

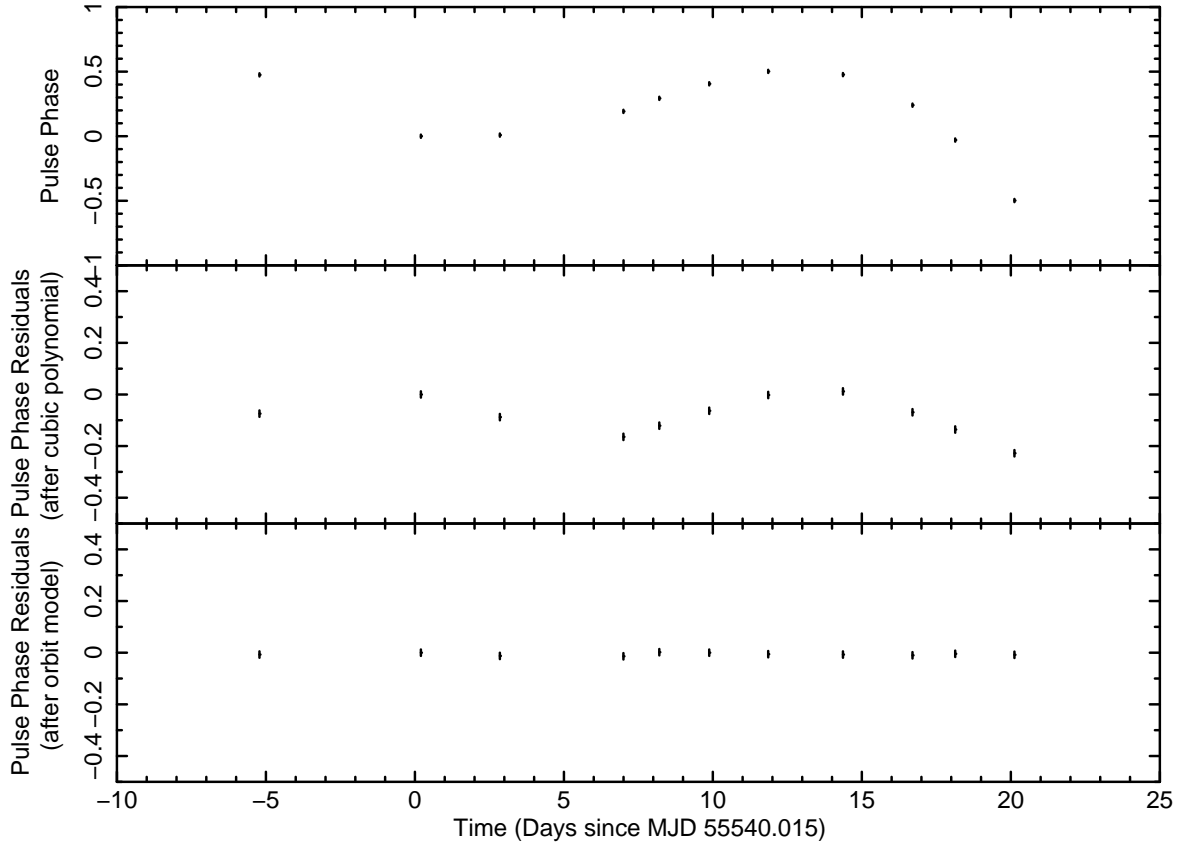


**Figure 2.** (Top) Pulse phases of MAXI J1409-619. (Middle) Residuals of pulse phases after removal of a cubic polynomial. (Bottom) Residuals of pulse phases after removal of the orbit model.

In Fig. 3, we take time slopes of pulse arrival times and present the pulse frequencies together with Fermi observations.

The residuals of the cubic polynomial fit can alternatively be expressed as the noise process due to random torque fluctuations (Bildsten et al. 1997; Baykal et al. 2007). We estimate the noise strength by using the root mean square (rms) residuals of cubic polynomial fit (Cordes 1980; Deeter 1984). In general, for the  $r^{th}$ -order red noise (or  $r^{th}$  order integral of white noise) with strength  $S_r$ , the mean square residual for data spanning an interval with length  $T$  is proportional to  $S_r T^{2r-1}$ . The expected mean square residual, after removing a polynomial of degree  $m$  over an interval of length  $T$ , is given by

$$\langle \sigma_R^2(m, T) \rangle = S_r T^{2r-1} \langle \sigma_R^2(m, 1) \rangle_u, \quad (3)$$

where the  $\langle \sigma_R^2(m, 1) \rangle_u$  is the normalization constant which can be estimated by measuring the variance of residuals by removing the degree of polynomial  $m$  for unit noise strength  $S_r$ . We use  $m=3$  for cubic polynomial and  $r=2$  for second order red noise in pulse arrival times (or pulse phases) which corresponds to first order red noise (or random walk) in pulse frequency. We estimate the normalization constant by Monte Carlo simulation of observed time series for second order red

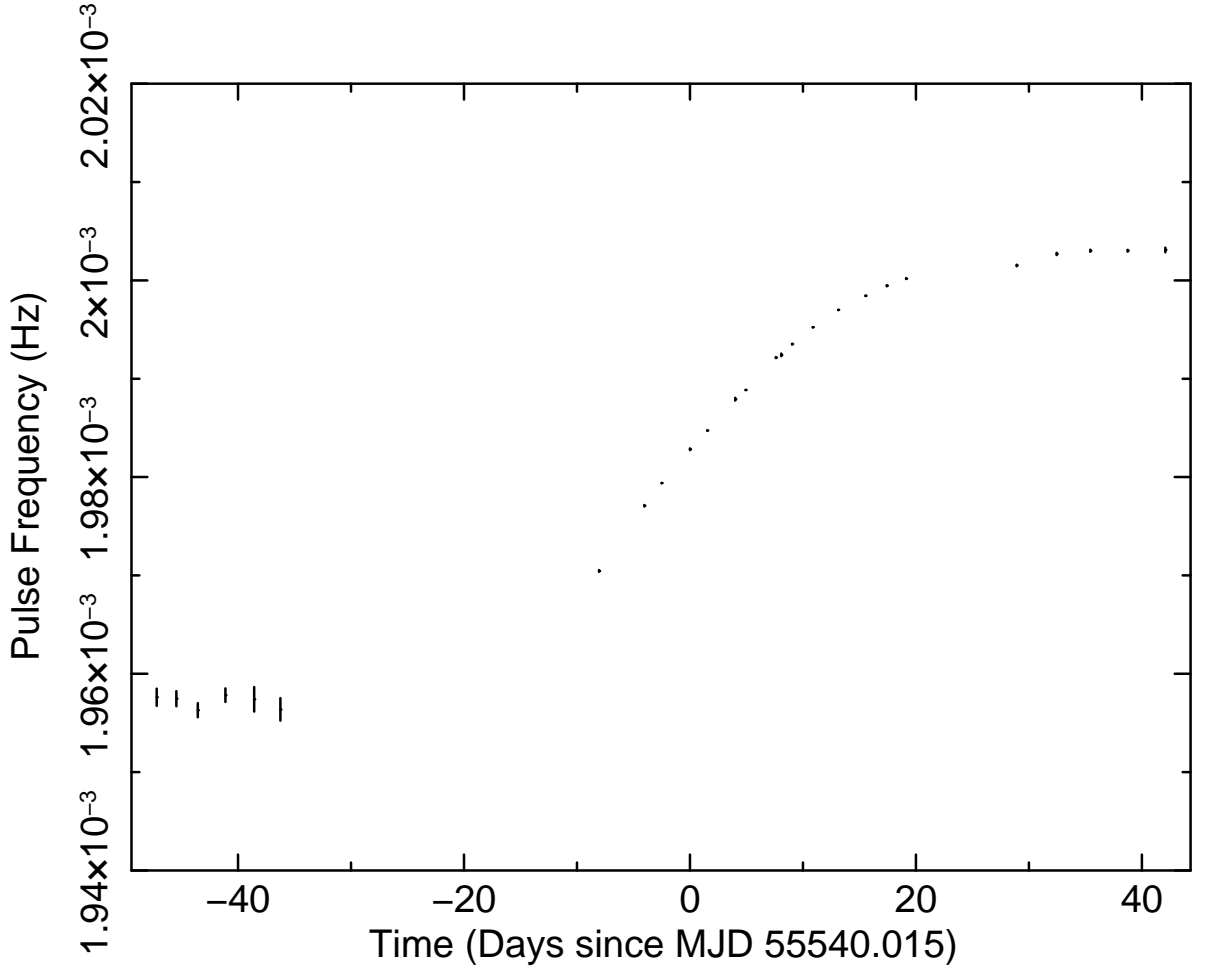


Figure 3. Frequency times series of MAXI J1409-619.

noise process ( $r = 2$ ), for a unit noise strength  $S(r = 2)$ . Our expected normalization constants are consistent with those obtained by direct mathematical evaluation (Deeter 1984; Cordes 1980).

Torque fluctuations and the noise of accretion powered pulsars have been studied for several sources (Baykal & Oegelman 1993; Bildsten et al. 1997). The torque noise strength is obtained for MAXI J1409-619 as  $1.3 \times 10^{-18} \text{ Hz s}^{-2}$ . This value of the noise strength estimate is on the same order with those of other accretion powered sources such as wind accretors e.g. Vela X-1, 4U 1538-52 and GX 301-2 with the values changing between  $10^{-20}$  and  $10^{-18} \text{ Hz s}^{-2}$  (Bildsten et al. 1997). Her X-1 and 4U 1626-67, which are disc accretors with low mass companions, have shown pulse frequency derivatives consistent with noise strengths  $10^{-21}$  to  $10^{-18} \text{ Hz sec}^{-2}$  (Bildsten et al. 1997). Therefore the residuals of the cubic polynomial fit can also be associated with torque noise fluctuation of the source.

**Table 1.** Timing Solution of MAXI J1409-619.

Parameter	Value
Epoch (Days in MJD)	55540.0150(6)
$\nu$ ( $10^{-3}$ Hz)	1.98287(4)
$\dot{\nu}$ ( $10^{-11}$ Hz s $^{-1}$ )	1.599(9)
$\ddot{\nu}$ ( $10^{-18}$ Hz s $^{-2}$ )	-6.4(8)
Orbital Period (Days)	14.7(4)
$a/c \sin i$ (s)	25.7(5)
Orbital Epoch (Days in MJD)	55547.5375(6)

### 3.2.1 Torque–luminosity correlations

Using RXTE-PCA observations between MJD 55531 and MJD 55575 corresponding to the high luminosity region of the lightcurve, for which a temporary accretion disc formation is plausible, we investigate the relation between torque and X-ray luminosity of the source using pulse frequency derivative and count rate measurements each corresponding to two-day long intervals.

If the source accretes via an accretion disc, the standart accretion disc theory (Ghosh & Lamb 1979; Wang 1987; Ghosh 1994; Li & Wickramasinghe 1998; Dai & Li 2006) suggests a relation between total external torque exerted on the neutron star and the bolometric luminosity of the source. For this case, radius of inner edge of the accretion disc gets ( $r_0$ ) smaller as the accretion rate ( $\dot{M}$ ) increases and can be approximated as (Pringle & Rees 1972; Lamb et al. 1973),

$$r_0 = K\mu^{4/7}(GM)^{-1/7}\dot{M}^{-2/7}, \quad (4)$$

where  $\mu$  is the magnetic moment of the neutron star ( $\mu \simeq BR^3$ ,  $B$  is the surface magnetic field and  $R$  is the radius of the neutron star),  $G$  is the universal gravitational constant,  $M$  is the mass of the neutron star and  $K$  is a dimensionless parameter of the order of unity.

Total external torque estimate due to accretion can then be expressed as (Ghosh & Lamb 1979),

$$2\pi I\dot{\nu} = n(\omega_s)\dot{M}l_K, \quad (5)$$

where  $l_K = (GMr_0)^{1/2}$  is the angular momentum per unit mass added by the disc to the neutron star at radius  $r_0$  and  $I$  is the moment of inertia of the neutron star. In this equation,  $n(\omega_s)$ , called "dimensionless torque", is approximately given by

$$n(\omega_s) \approx 1.4(1 - \omega_s/\omega_c)/(1 - \omega_s). \quad (6)$$



In the above equation,  $\omega_s$  is the fastness parameter, which is equal to the ratio of the spin frequency of the neutron star to the Keplerian frequency at  $r_0$  radius which can further be expressed as

$$\omega_s = v/v_K(r_0) = 2\pi K^{3/2} P^{-1} (GM)^{-5/7} \mu^{6/7} \dot{M}^{-3/7}, \quad (7)$$

and  $\omega_c$  is the critical fastness parameter with a value of  $\sim 0.35$ .

Due to the release of gravitational potential energy of the accreted material, X-ray emission with a luminosity of

$$L = \eta GM \dot{M} / R, \quad (8)$$

occurs at the neutron star surface. In this equation,  $\eta$  is a dimensionless efficiency factor typically close to and smaller than unity. Using Eqns. 4, 5 and 8, the relation between spin frequency derivative and X-ray luminosity can be written as,

$$\dot{\nu} = \frac{n(\omega_s)}{2\pi I} K^{1/2} (GM)^{-3/7} \mu^{2/7} R^{6/7} L^{6/7}. \quad (9)$$

Eqn. 9 indicates a linear relationship between frequency derivative and 6/7th power of luminosity in cases of the presence of strong material torques giving rise to a positive dimensionless torque magnitude of which is close to unity. In Fig. 4, it is evident that count rate is directly proportional to the 6/7th power of X-ray count rate which is an indication of the relation between frequency derivative and 6/7th power of luminosity with the assumption that luminosity from 2-60 keV should correspond to most of the X-ray emission from this source.

The slope of a linear fit of Fig. 4 is found to be  $1.07 \times 10^{-13} \text{ (Hz/s)(counts/s)}^{-6/7}$ . Using Eqns. 4 - 9 and assuming a distance of 15 kpc (Orlandini et al. 2012), this slope corresponds to an  $r_0$ ,  $n(\omega_s)$  and surface magnetic field strengths of  $4.83 \times 10^8$  cm, 1.37 and  $2.87 \times 10^{11}$  Gauss respectively.

### 3.2.2 QPOs

We detected QPOs at 0.1–0.2 Hz range, and harmonic features of QPOs in the power spectra of MAXI J1409-619, which evolve over time. We perform our QPO analysis using our Python code.

To create power spectra from the RXTE-PCA lightcurve, POWSPEC tool is used. During the power spectrum generation, the lightcurve is divided into 256 s long time intervals, each of which contains 1024 bins with 0.25 second rebinning time. Each consecutive 9 intervals are averaged into one frame, therefore each power spectrum plot spans 2304 seconds. Then, the results are rebinned by a factor of 4.

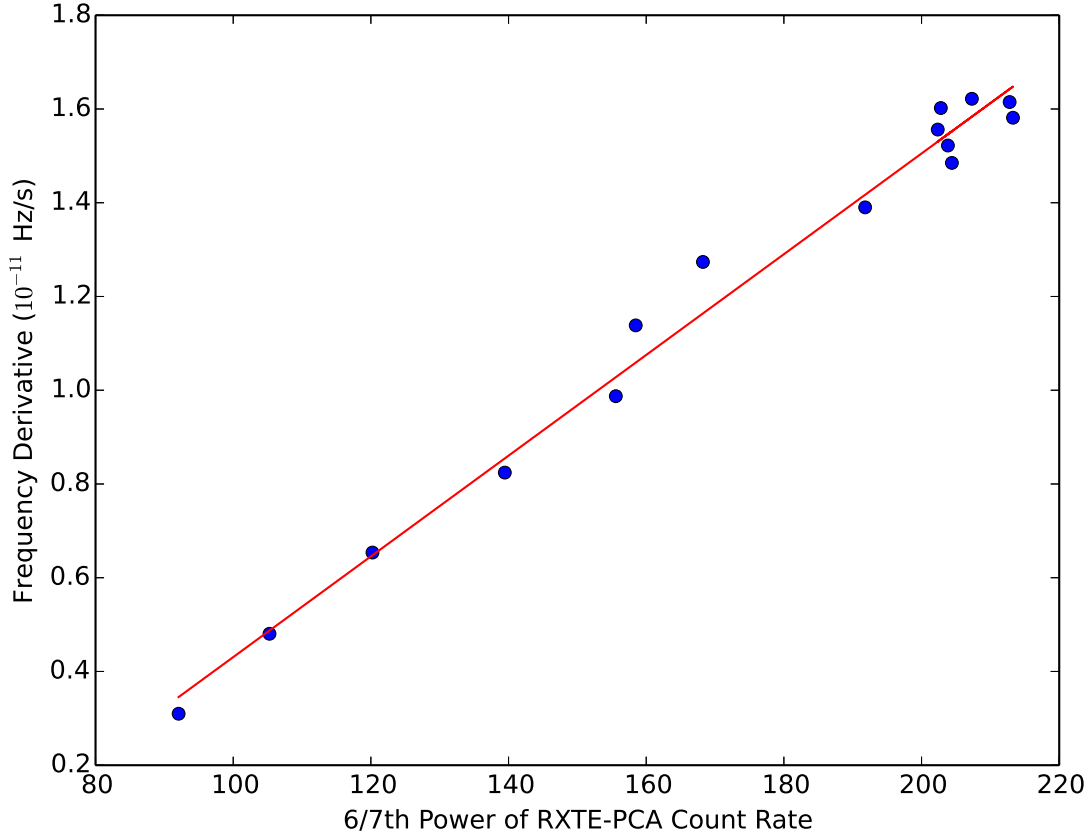


**Figure 4.** Measured frequency derivatives from RXTE-PCA observations as a function of 6/7th the power of 2-60 keV RXTE-PCA count rate. Solid line indicates the best linear fit.

The continuum of the power spectra is represented by a smoothly broken power law mode, which is defined as

$$f(x) = A \left( \frac{x}{x_b} \right)^{-\alpha_1} \left\{ \frac{1}{2} \left[ 1 + \left( \frac{x}{x_b} \right)^{\frac{1}{\Delta}} \right] \right\}^{(\alpha_1 - \alpha_2)\Delta} \quad (10)$$

where  $A$  is the amplitude,  $x$  is the frequency,  $x_b$  is the break frequency,  $\alpha_1$  and  $\alpha_2$  are the power law indices at frequency  $f < x_b$  and  $f > x_b$ , respectively, and  $\Delta$  is the smoothness parameter<sup>2</sup>. The QPOs are seen as excess peaks in the continuum and can be modeled as Lorentzian components added to the base continuum model. The additive Lorentzian component is defined as

$$L = \frac{l_n}{1 + \left( 2 \times \frac{x - l_c}{l_w} \right)^2} \quad (11)$$

where  $x$  is the frequency,  $l_n$  is the line normalization parameter,  $l_c$  is the center frequency of the

<sup>2</sup> <http://docs.astropy.org/en/stable/api/astropy.modeling.powerlaws.SmoothlyBrokenPowerLaw1D.html>

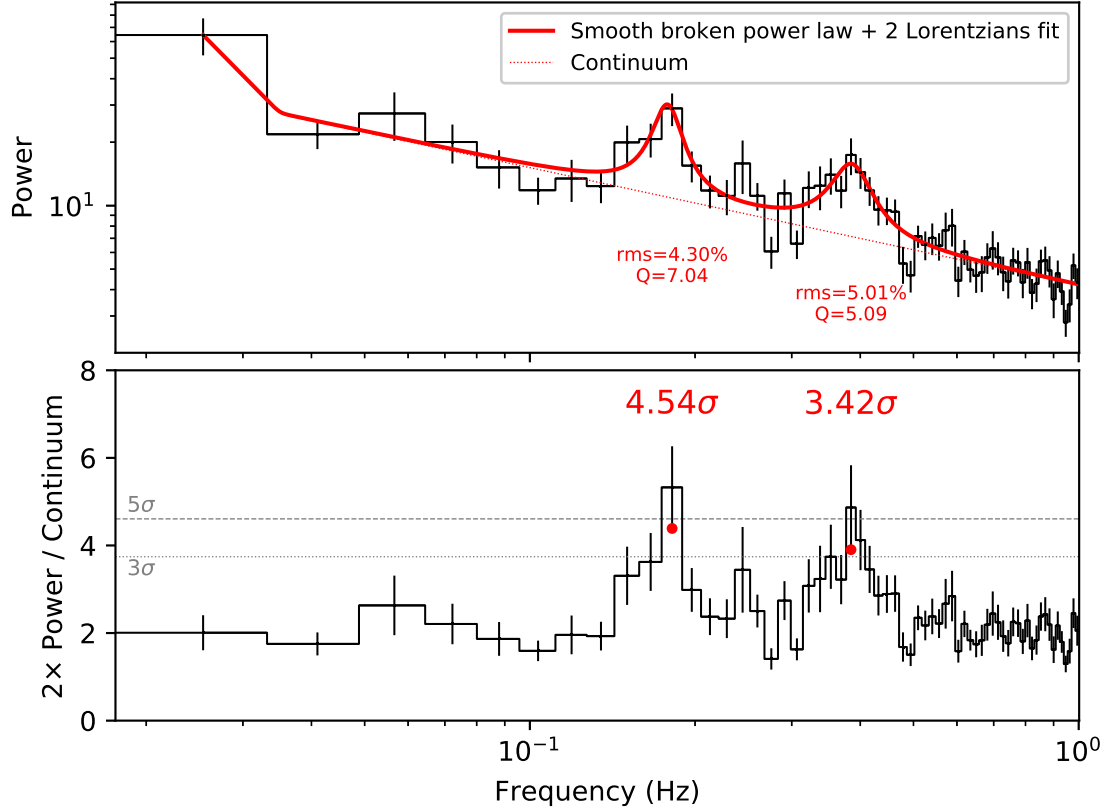


**Figure 5.** The power spectrum fit of the first 2304-second-long segment of observation 95441-01-01-06, conducted in MJD 55545.

line, and  $l_w$  is the line width<sup>3</sup>. Appearing harmonic peaks of QPO frequency are modeled with additional Lorentzian components. Our Python code resolves the optimal parameters for the fit and returns the error range of the parameters within  $1\sigma$  level.

The significance of the QPO features are calculated by normalizing the power spectrum by dividing by modeled continuum and multiplying the result by 2 (van der Klis 1988). The resulting power spectrum would be consistent with a  $\chi^2$  distribution for  $2 \times 4 \times 9 = 72$  degrees of freedom (dof). As an example, an excess power of 4 corresponds to a total power of  $4 \times 4 \times 9 = 144$ , and the probability of having a false signal is calculated as  $Q(144|72) = 1.01 \times 10^{-6}$ . We have 252 frequencies in each power spectra, therefore the total probability of having a false signal is calculated as  $252 \times 1.01 \times 10^{-6} = 2.53 \times 10^{-4}$ , which corresponds to  $3.66\sigma$  level of detection. We selected QPOs and their harmonics with more than  $3\sigma$  significance, seen at Figure 6. One example of a power spectra fit and corresponding QPOs is shown in Figure 5.

<sup>3</sup> <https://wwwastro.msfc.nasa.gov/qdp/help/model.html>

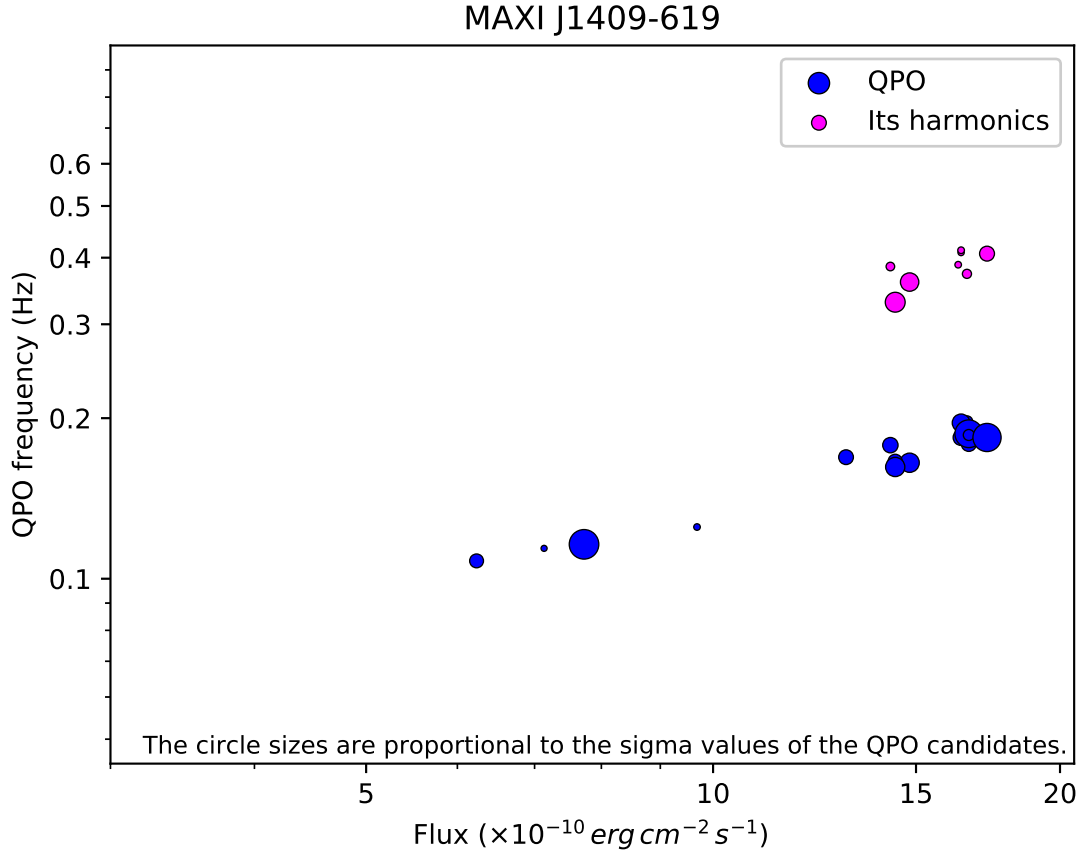


**Figure 6.** QPO centroid frequencies versus flux. QPOs with only more than  $3\sigma$  significance are included. The biggest circle in the plot amounts to  $6.90\sigma$ .

QPOs are detected only at the first half of the outburst stage in 2010 December. QPO amplitudes fluctuate substantially over time, and occasionally, QPO features disappear altogether in power spectra. QPO harmonics seem to appear for the most cases, found around double the centroid frequency of the main QPO features, though many of these harmonics are not statistically significant.

Another notable result is that the QPO centroid frequencies decrease consistently over time. The first QPOs are detected around 0.2 Hz; however, as the outburst flux decays, QPO centroid frequencies decrease down to 0.1 Hz (see Figure 6). As the source flux consistently decreases over time in the time period where the QPOs are detected, we can conclude that QPO centroid frequencies decrease linearly with flux.

### 3.2.3 Pulsed fractions

Using RXTE-PCA lightcurve, we calculate pulsed fraction of the source for each observation. For our calculations, we use 20 binned pulse profiles and used the definition  $P.F. = (I_{max} -$

[!t]

**Table 2.** Detected QPOs of MAXI J1409-619.

Epoch (MJD)	$\nu_{QPO}$ (Hz)		Q-factor		Significance ( $\sigma$ )	
	#1	#2	#1	#2	#1	#2
55541.621	0.197±0.003	-	6.340	-	3.934	-
55541.648	0.189±0.002	0.373±0.003	6.751	18.672	3.103	3.510
55541.804	0.196±0.003	0.409±0.009	7.788	4.311	4.934	3.044
55541.831	-	0.413±0.006	-	20.630	-	3.103
55541.957	0.184±0.002	-	8.924	-	4.636	-
55542.665	0.179±0.003	-	3.620	-	4.491	-
55542.709	0.187±0.001	-	8.862	-	6.590	-
55542.785	0.186±0.002	-	4.279	-	3.822	-
55543.818	0.184±0.001	-	7.895	-	6.667	-
55543.845	-	0.407±0.003	-	19.310	-	4.467
55544.798	-	0.388±0.007	-	4.580	-	3.087
55545.638	0.178±0.002	0.385±0.006	7.036	5.089	4.543	3.421
55546.835	0.165±0.003	0.360±0.002	3.042	11.423	5.191	5.045
55547.097	0.166±0.003	0.330±0.005	2.430	4.644	4.348	5.291
55547.124	0.162±0.002	-	6.661	-	5.186	-
55549.395	0.169±0.002	-	5.096	-	4.439	-
55554.353	0.125±0.002	-	5.388	-	3.089	-
55556.705	0.116±0.001	-	4.930	-	6.897	-
55558.142	0.114±0.001	-	5.253	-	3.003	-
55559.644	0.108±0.005	-	5.036	-	4.294	-

$I_{min})/(I_{max} + I_{min})$ , where  $I_{min}$  and  $I_{max}$  are the count rates of the bins with the minimum count rate and the maximum count rate respectively.

In order to figure out the flux dependence of pulsed fraction of the source, we plot these measurements as a function of RXTE-PCA count rate of the source in Fig. 7.

### 3.3 Spectral Analysis

#### 3.3.1 Time-resolved spectra

Swift XRT has a moderate spectral resolution and no single observation of it has an exposure of more than 2 ks, therefore observations close in time and having similar count rates are combined into 6 groups in order to increase the statistical significance of the resulting spectra. The spectra are binned with a minimum of 5 counts per bin, and C statistic (*cstat*) is used in *xspec*. The spectra are fitted simply with a photoelectric absorption  $\times$  power law (*phabs\*powerlaw*) model. The 90% confidence ranges of the fit parameters are calculated with *uncer* command, and the flux of the entire model is calculated with the command *cflux*. The given model successfully fits the spectra, yet the spectral quality is inferior compared to RXTE-PCA data (see Figure 8). The evolution of the parameters are consistent those obtained using the analysis of RXTE-PCA data, but due to the amount of Swift-XRT data available, there are only 6 statistically modellable spectra within 100 days. The reduced chi-squared values of the fits are between 0.72 and 1.21. Results of spectral fitting of Swift-XRT observations are given in Table 3.

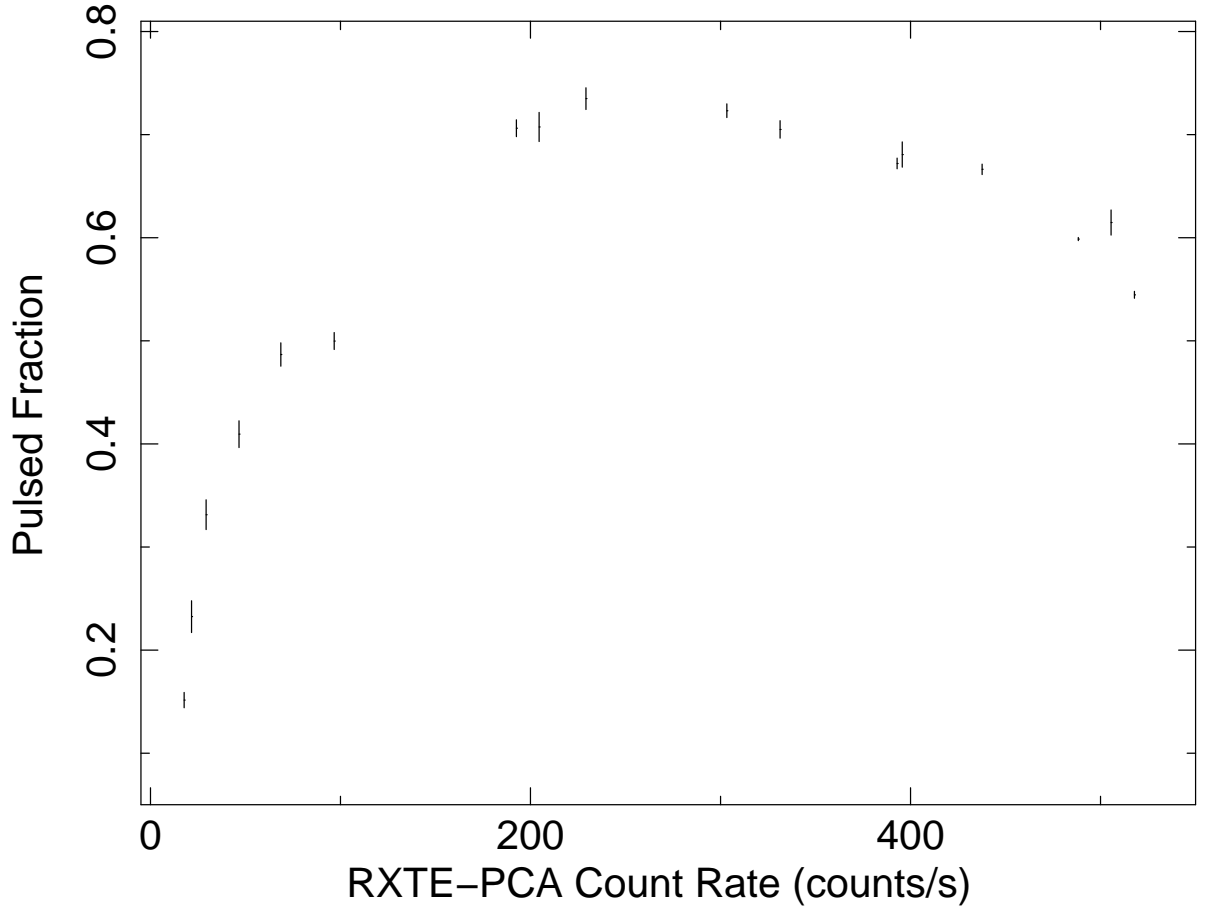


**Figure 7.** Pulsed fraction as a function of 2-60 keV RXTE-PCA count rate of the source.

[!h]

**Table 3.** Spectral fitting parameters of Swift XRT data. Note that flux values are in terms of  $10^{-10}$  erg s $^{-1}$  cm $^{-2}$ .

	Group 1	Group 2	Group 3	Group 4	Group 5	Group 6
Obs. midtime (MJD)	55490.89	55493.19	55498.34	55502.52	55530.86	55583.68
$\Sigma$ duration (s)	3590	3305	2111	2051	2597	4615
$n_H$ ( $\times 10^{22}$ cm $^{-2}$ )	$5.43^{+0.74}_{-0.66}$	$3.78^{+0.98}_{-0.86}$	$2.99^{+1.11}_{-0.96}$	$5.35^{+1.65}_{-1.41}$	$5.21^{+0.63}_{-0.59}$	$9.08^{+4.44}_{-3.47}$
Photon index	0.73	$0.73^{+0.32}_{-0.31}$	$0.30^{+0.36}_{-0.35}$	$1.03^{+0.46}_{-0.43}$	$0.89^{+0.18}_{-0.18}$	$1.78^{+1.00}_{-0.90}$
Hardness ratio	2.29	2.28	3.80	1.56	1.86	0.48
Flux	$1.38^{+0.12}_{-0.11}$	$1.17^{+0.10}_{-0.10}$	$2.02^{+2.64}_{-1.11}$	$1.68^{+0.19}_{-0.17}$	$8.61^{+0.40}_{-0.39}$	$0.13^{+0.06}_{-0.03}$
Reduced $\chi^2$	1.0615	1.1150	0.9286	0.7237	0.99558	1.163

For RXTE-PCA spectral analysis, we first combine and fit all observations in 95441 set (74.4 ks) resulting in a single spectrum. While fitting, a systematic error of 0.5% is set. Among the different models, an absorbed power law with a high energy cutoff plus a Gaussian iron line fixed at 6.4 keV ( $phabs*(cutoffpl+gauss)$ ) gives the most plausible results (see Figure 9).

Afterwards, the observations are fitted separately in order to investigate the evolution of the fit parameters over time. Subsequent short observations are combined before fitting when the exposure times are insufficient leading to 37 statistically modellable spectra. Most of the spectra are fitted with a cutoff model. However, as the count rates of the observations decrease, decreasing

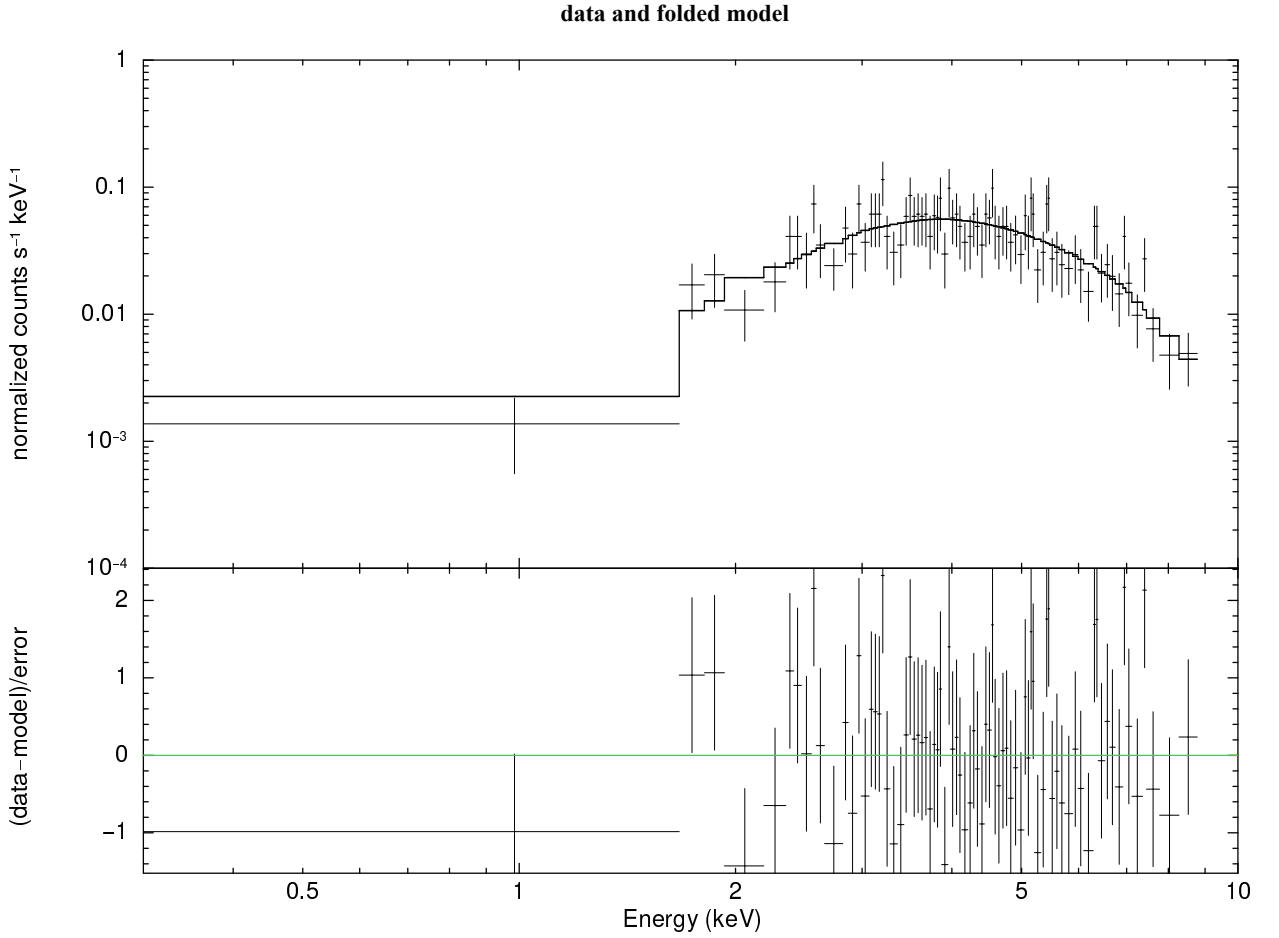


**Figure 8.** Swift XRT spectrum of MAXI J1409-619 with power law model (MJD 55501–55503; Group 4 in Table 3).

signal-to-noise ratio deteriorates the spectral quality, causing difficulties in finding cutoff energies. Therefore some spectra are fitted with a power law model without the cutoff model. Additionally, a 0.5% systematic error is set while fitting spectra of combined or long-duration observations. The evolution of the parameters are presented in Figure 10.

In general, the models accurately fit the spectra: Only two spectra have  $\chi^2$  values exceeding 2. Photon index values exhibit an inverse proportional relation with flux to a certain degree, after which photon index values stay relatively flat. This relation is shown in Figure 11. High energy cutoff values are only obtained at the outburst stage, and are decreasing over time. At the pre-outburst stage and the tail of the outburst, statistically meaningful cutoff values cannot be found.

Especially in long observations, a bump around 10 keV is seen in fit residuals. This feature was mentioned by Coburn et al. (2002) and it was also observed in many accreting X-ray pulsars, not only in RXTE data but also Ginga and BeppoSAX data. Being always at around 10 keV, the feature is not considered to be a cyclotron line or another absorption feature, therefore it was concluded that it might be an innate feature common in accreting pulsars. Using NPEX model is considered

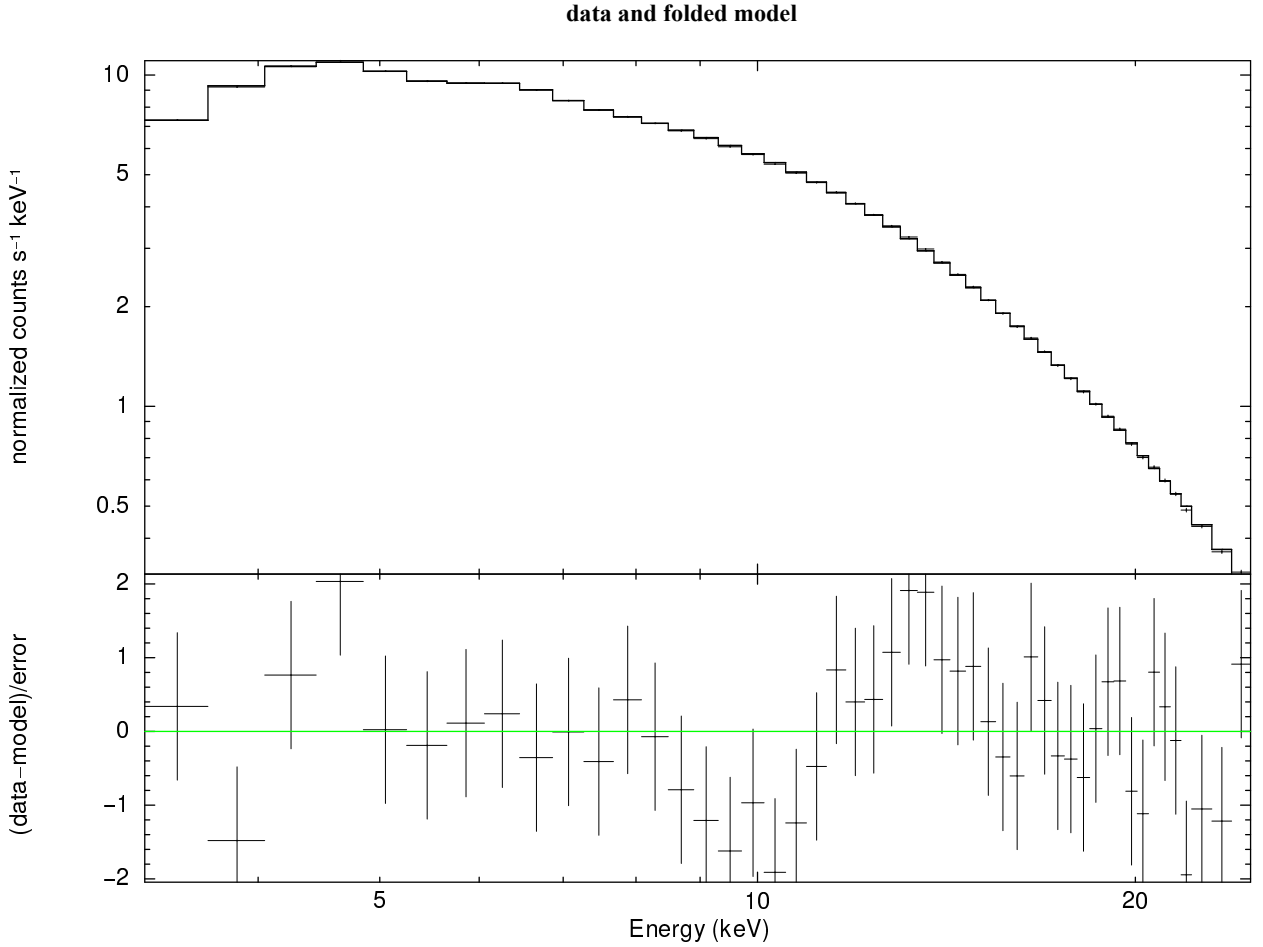


**Figure 9.** RXTE PCA spectrum of the whole 95441 set (MJD 55540–55560, 74.4 ks) is best fitted with power law with a high energy cutoff plus a Gaussian iron line fixed at 6.4 keV.

as a possible workaround, nonetheless it is not completely successful at eliminating the feature and is not used as a final solution.

### 3.3.2 Pulse-phase-resolved spectra

We performed pulse-phase-resolved spectral analysis for the 3 observations conducted on 2010 December 11–12 (MJD 55541–55542) where the outburst is at its maximum, totaling 34.0 ks. A spin period of 503.62 s (1.9856 mHz) is used which is found from timing analysis. A total of 10 phase bins are used; as a result, spectrum of each phase bin has been obtained from about 3.4 ks of exposure, which is found to be sufficient for statistically meaningful analysis. The phase resolved spectra are fitted by an absorbed power law with a high energy cutoff plus a Gaussian iron line fixed at 6.4 keV.

The pulse phase dependence of the spectral parameters are presented in Figure 12. The double peaked nature of the pulse profile is evident in phase dependent flux measurements. The neutral hydrogen column density  $n_H$  does not have a significant variation with changing phase. The



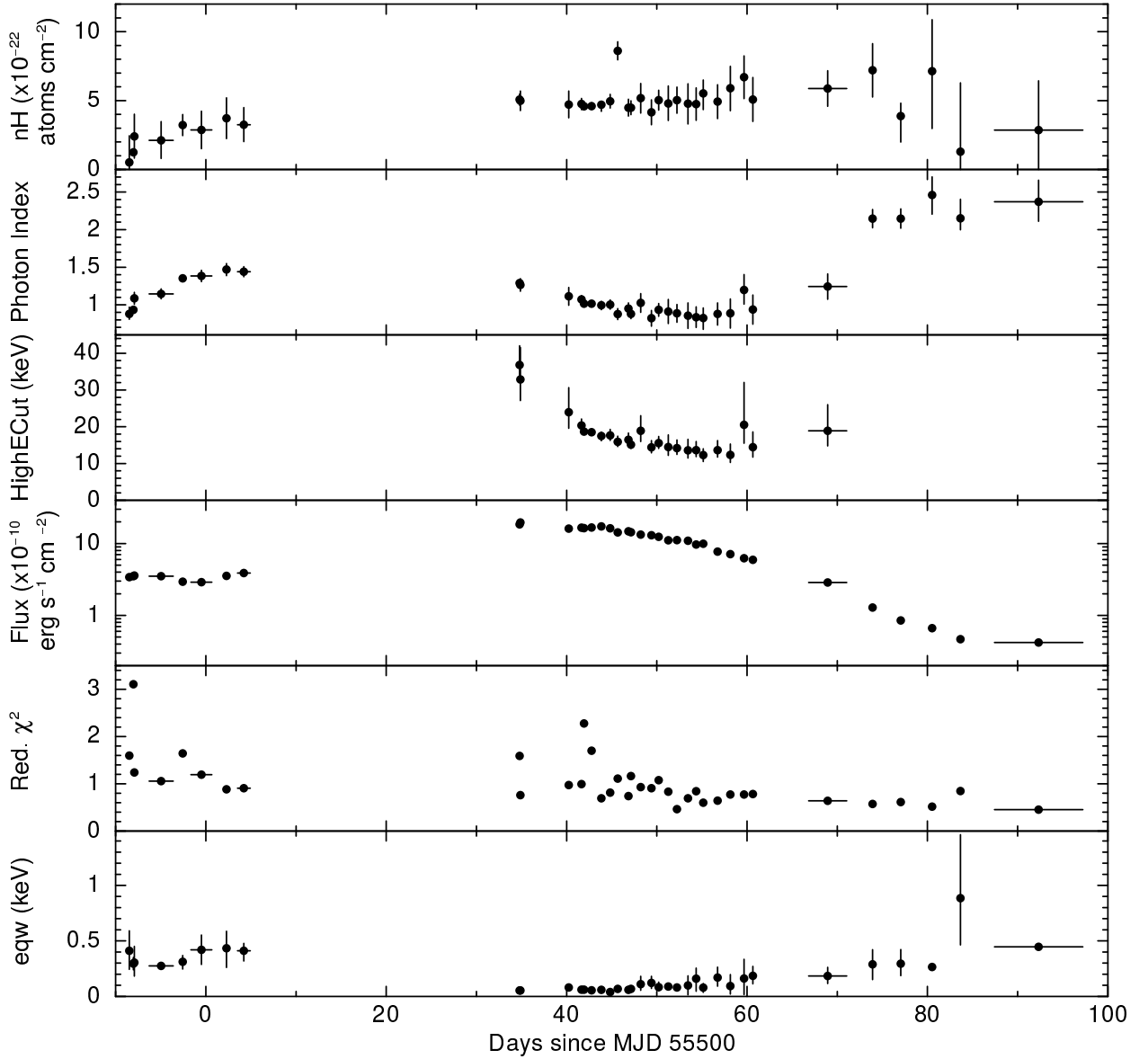


**Figure 10.** The evolution of the fitting parameters of RXTE PCA observations over time.

photon index appears to be low during the pulse peaks, and goes up notably when the flux is minimum. Higher photon index values at the minimum flux can be explained by hard emission of the pulsed flux. When the pulsed flux diminishes, the observed emission is softened. At the pulse minima, the high energy cutoff value goes out of 3–25 keV range. This is probably the result of the decreased signal-to-noise ratio due to decreased count rate of the source. Besides, the phase bins corresponding to the pulse minimas have larger  $\chi^2$  values, possibly owing to the excess high-energy cutoff values obtained by the fit and the smaller signal-to-noise ratios as explained above. Broadening of the Gaussian line might be explained by blending of two iron lines at pulse minimum: When the enhanced emission of the hot spots fades from view,  $K\beta$  line emission at 7.04

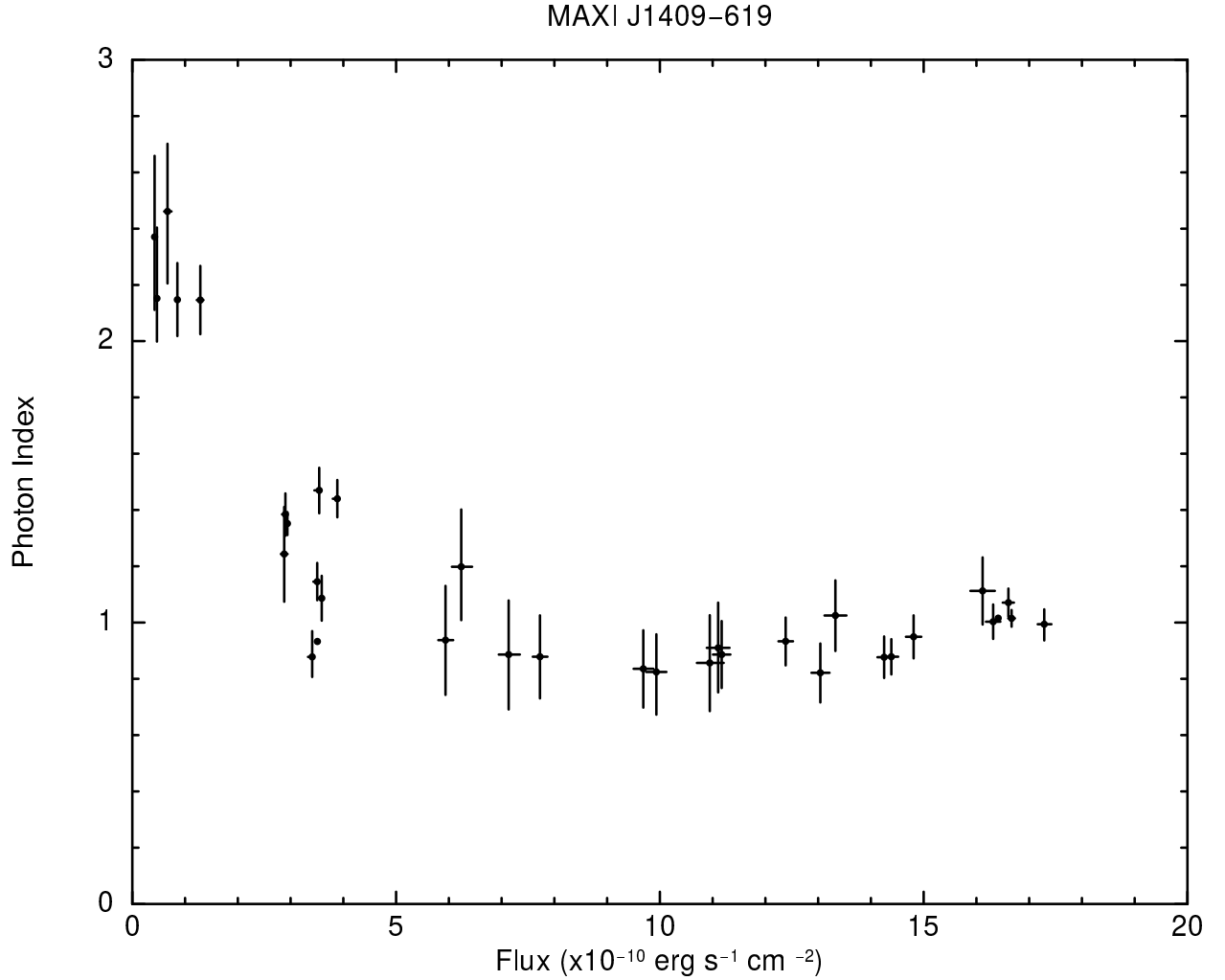


**Figure 11.** The relation between photon indices and fluxes of RXTE PCA observations.

keV emerges alongside the  $K\alpha$  line emission at 6.4 keV, resulting the aforementioned broadening (Serim et al. 2017).

### 3.3.3 Energy Dependent Pulse Profiles

In addition to the pulse profile shown in the uppermost panel of Figure 12, energy dependence of pulse profiles are also investigated (see Figure 13).

Apparently, the pulse profile of MAXI J1409-619 do not exhibit strong energy dependence, however, the pulsed fraction alters in different bands. While it is most prominent in 8-13 keV energy range, it diminishes at higher energies, almost vanishing above 25 keV.

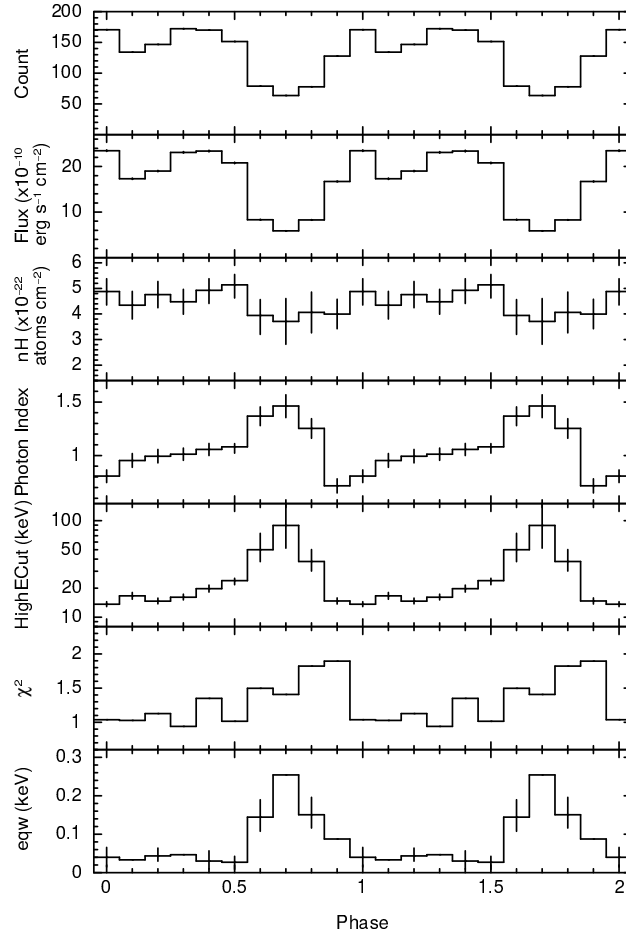


**Figure 12.** Evolution of count rates, flux, hydrogen column density, photon index, cut-off energy, reduced  $\chi^2$ , and equivalent width of the Gaussian component over phase in MJD 55541–55542.

#### 4 SUMMARY AND DISCUSSION

Using RXTE-PCA and SWIFT-XRT observations of MAXI J1409-619, we perform timing and X-ray spectral analysis, probing new insights about the nature of this transient source.

After fitting pulse arrival times to a cubic polynomial, we have found that the corresponding residuals indicate a possible circular orbit with an orbital period of 14.9(7) days. This orbital model has indicated a mass function of about  $0.1M_{\odot}$  implying that the orbital inclination angle should be very small. We have also provided an alternative interpretation of these residuals as the noise process due to random torque fluctuations which leads to a torque noise strength estimation of  $1.3 \times 10^{-18} \text{ Hz s}^{-2}$  which is on the same order with some wind accreting accretion powered pulsars in HMXB systems and some disc accreting accretion powered pulsars in LMXB systems.

We have considered the correlation between pulse frequency derivative and X-ray count rate (see Figure 4) as a consequence of disc accretion. Using standard accretion disc theory, we have estimated the inner disc radius and surface dipole magnetic field strength as about  $4.8 \times 10^8 \text{ cm}$  and

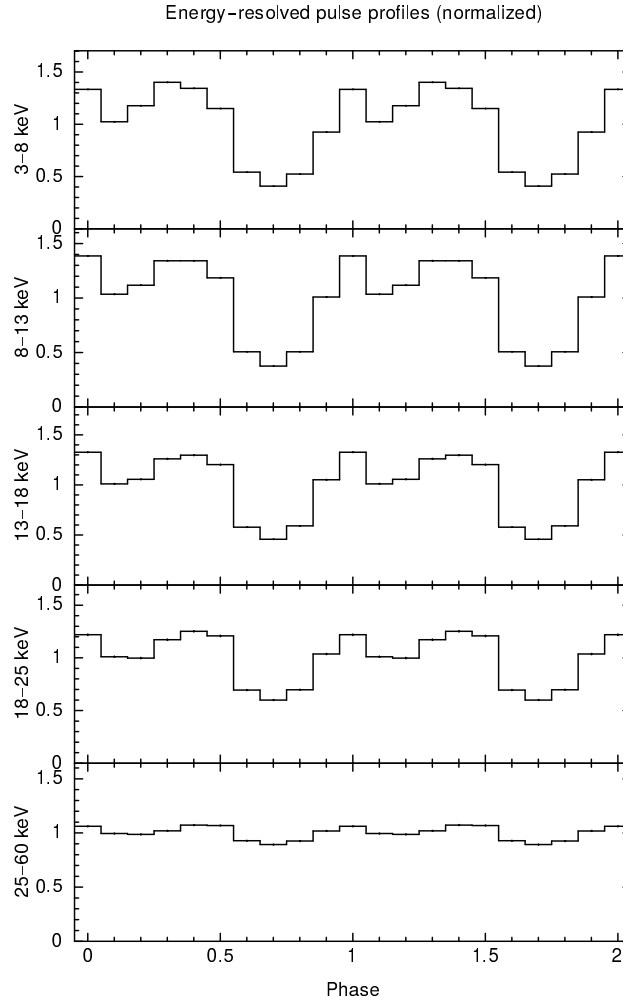


**Figure 13.** Normalized energy-resolved pulse profiles of RXTE PCA observations in MJD 55541–55542.

$2.9 \times 10^{11}$  Gauss respectively. Our magnetic field strength estimate is about one order smaller than the previous estimate of  $\approx 3.8 \times 10^{12}$  Gauss obtained from cyclotron resonance spectral feature (Orlandini et al. 2012)

QPOs with a very wide range of peak frequencies from 0.01 Hz to 0.4 Hz have been observed in many accretion powered pulsars (see Acuner et al. (2014), İnam et al. (2004) and references therein). MAXI J1409-619 is unique, being the first source observed to have harmonics of its QPO feature (Dugair et al. 2013). Currently, 4U 0115+63 together with MAXI J1409-619 are the only two accreting X-ray pulsars known to show QPO harmonics (Roy et al. 2019).

QPOs have usually been interpreted either as the Keplerian frequency at the inner radius of the accretion disc (van der Klis et al. 1987) or the beat frequency of the Keplerian frequency at the inner radius of the accretion disc and the spin period of the neutron star (Lamb et al. 1985).

As seen from Figure 6, centroid frequencies of detected QPOs decrease from 0.2 Hz to 0.1 Hz consistently with decreasing X-ray flux while outburst flux decays. Since these frequencies are

much greater than the spin frequency of the source, we can solely interpret them to be equal to the Keplerian frequencies at the inner radius of the accretion disc while the inner disk varies with decreasing X-ray flux and then the inner disk radius can be related to the QPO centroid frequency ( $\nu_{QPO}$ ) as

$$r_0 = \left[ \frac{(GM)^{1/2}}{2\pi\nu_{QPO}} \right]^{2/3}. \quad (12)$$

From Equation 12, our QPO frequencies indicate that the inner radius of the accretion disc moved outward from  $r_0 = 4.9 \times 10^8$  cm to  $r_0 = 7.8 \times 10^8$  cm as the outburst faded. This range of inner disk radii is on the same order with the one estimated using torque luminosity correlation ( $r_0 = 4.8 \times 10^8$  cm) thus is reasonably compatible with our magnetic field strength estimation of  $2.9 \times 10^{11}$  Gauss.

From Figure 7, pulsed fraction of the source is found to be correlated with the RXTE-PCA count rate of the source up to 200 counts/s corresponding to a 2-60 keV luminosity of about  $5 \times 10^{37}$  ergs  $s^{-1}$  assuming a distance of 15 kpc. Beyond this luminosity level, pulsed fraction marginally decreases with increasing count rate. The correlation seen in lower count rates should be due to the increased efficiency of accretion with increasing mass accretion rate onto the magnetic poles resulting in a higher pulsed fraction as observed for the source XMMU J054134.7–682550 (Inam et al. 2009). On the other hand, for luminosities higher than  $\sim 5 \times 10^{37}$  ergs  $s^{-1}$ , the marginal anti-correlation between count rate and pulsed fraction is similar to the case of a super-Eddington accretor ultra luminous X-ray source NGC7793 P13 (Walton et al. 2018) for which the presence of two emission components contributing (pulsed and non-pulsed) to total luminosity and the relative contribution from the pulsed component is lower at higher luminosities.

We have presented spectral analysis of Swift-XRT and RXTE-PCA observations of the source. Temporal evolution of X-ray spectral parameters of the source using RXTE-PCA observations is given in Figure 10. From Figure 11, photon index doesn't vary significantly with RXTE-PCA flux except for the lowest X-ray fluxes ( $< 2 \times 10^{-10}$  ergs  $s^{-1}$   $cm^{-2}$  corresponding to an upper limit of X-ray luminosity of about  $5 \times 10^{36}$  ergs  $s^{-1}$ ) for which power law index is significantly higher indicating a softer spectrum.

From the phase resolved spectrum of the source (see Figure 12), we have also shown that phases with lower flux tend to have higher power law index (i.e. have softer spectra).

**ACKNOWLEDGEMENTS**

We acknowledge support from TÜBİTAK, the Scientific and Technological Research Council of Turkey through the research project MFAG 118F037.

**REFERENCES**

- Acuner Z., İnam S. Ç., Şahiner Ş., Serim M. M., Baykal A., Swank J., 2014, *MNRAS*, **444**, 457
- Baykal A., Oegelman H., 1993, *A&A*, **267**, 119
- Baykal A., İnam S. Ç., Stark M. J., Heffner C. M., Erkoca A. E., Swank J. H., 2007, *MNRAS*, **374**, 1108
- Bildsten L., et al., 1997, *ApJS*, **113**, 367
- Burrows D. N., et al., 2005, *Space Science Reviews*, **120**, 165
- Camero-Arranz A., Finger M. H., Jenke P., 2010, *The Astronomer's Telegram*, **3069**, 1
- Coburn W., Heindl W. A., Rothschild R. E., Gruber D. E., Kreykenbohm I., Wilms J., Kretschmar P., Staubert R., 2002, *The Astrophysical Journal*, **580**, 394
- Cordes J. M., 1980, *ApJ*, **237**, 216
- Dai H. L., Li X. D., 2006, *A&A*, **451**, 581
- Deeter J. E., 1984, *ApJ*, **281**, 482
- Deeter J. E., Boynton P. E., 1985, in Hayakawa S. and Nagase F. Proc. Inuyama Workshop: Timing Studies of X-Ray Sources p.29, Nagoya Univ., Nagoya
- Dugair M. R., Jaisawal G. K., Naik S., Jaaffrey S. N. A., 2013, *MNRAS*, **434**, 2458
- Gehrels N., et al., 2004, *ApJ*, **611**, 1005
- Ghosh P., 1994, in Holt S., Day C. S., eds, American Institute of Physics Conference Series Vol. 308, The Evolution of X-ray Binaries. p. 439, doi:10.1063/1.45984
- Ghosh P., Lamb F. K., 1979, *ApJ*, **234**, 296
- İçdem B., Baykal A., İnam S. Ç., 2012, *MNRAS*, **419**, 3109
- İnam S. Ç., Baykal A., Swank J., Stark M. J., 2004, *ApJ*, **616**, 463
- İnam S. Ç., Townsend L. J., McBride V. A., Baykal A., Coe M. J., Corbet R. H. D., 2009, *MNRAS*, **395**, 1662
- Jahoda K., Swank J. H., Giles A. B., Stark M. J., Strohmayer T., Zhang W. W., Morgan E. H., 1996, *Proc.SPIE*, **2808**, 59
- Jahoda K., Markwardt C. B., Radeva Y., Rots A., Stark M. J., Swank J. H., Strohmayer T. E., Zhang W., 2006, *The Astrophysical Journal Supplement Series*, **163**, 401
- Kaur R., et al., 2010, *The Astronomer's Telegram*, **3082**, 1
- Kennea J. A., Krimm H., Romano P., Mangano V., Curran P., Evans P., 2010a, *The Astronomer's Telegram*, **2962**, 1
- Kennea J. A., Curran P., Krimm H., Romano P., Mangano V., Evans P. A., Yamaoka K., Burrows D. N., 2010b, *The Astronomer's Telegram*, **3060**, 1
- Lamb F. K., Pethick C. J., Pines D., 1973, *ApJ*, **184**, 271
- Lamb F. K., Shibazaki N., Alpar M. A., Shaham J., 1985, *Nature*, **317**, 681
- Leahy D. A., Elsner R. F., Weisskopf M. C., 1983, *ApJ*, **272**, 256
- Li J., Wickramasinghe D. T., 1998, *MNRAS*, **300**, 1015
- Orlandini M., Frontera F., Masetti N., Sguera V., Sidoli L., 2012, *ApJ*, **748**, 86
- Pringle J. E., Rees M. J., 1972, *A&A*, **21**, 1
- Roy J., et al., 2019, *ApJ*, **872**, 33
- Serim M. M., Āđahiner Ā., Çerri-Serim D., Āřnam S. Ç., Baykal A., 2017, *Monthly Notices of the Royal Astronomical Society*, **469**, 2509
- Sguera V., Orlandini M., Frontera F., Bazzano A., Bird A. J., 2010, *The Astronomer's Telegram*, **2965**, 1
- Ueno S., et al., 2010, *The Astronomer's Telegram*, **3067**, 1
- Walton D. J., et al., 2018, *MNRAS*, **473**, 4360

Wang Y. M., 1987, *A&A*, [183](#), 257

Yamamoto T., et al., 2010, *The Astronomer's Telegram*, [3070](#), 1

Yamaoka K., et al., 2010, *The Astronomer's Telegram*, [2959](#), 1

van der Klis M., 1988, in , NATO Advanced Study Institutes Series. Series C, Mathematical and Physical Sciences. Kluwer Academic Publishers, pp 27–70

van der Klis M., Stella L., White N., Jansen F., Parmar A. N., 1987, *ApJ*, [316](#), 411

This paper has been typeset from a  $\text{\TeX/L\AA\TeX}$  file prepared by the author.